

Research Article

Development and Fault Prediction of a New Operating Mechanism of HTPPM

Hongkui Yan^{1,2}, Xin Lin,¹ and Jianyuan Xu¹

¹Liaoning Province Key Laboratory of Power Grid Safe Operation and Monitoring, Shenyang University of Technology, Shenyang 110870, China

²School of Automation, Shenyang Institute of Engineering, Shenyang 110136, China

Correspondence should be addressed to Hongkui Yan; yanhk@126.com

Received 16 October 2020; Revised 27 January 2021; Accepted 18 April 2021; Published 26 April 2021

Academic Editor: Gordon Huang

Copyright © 2021 Hongkui Yan et al. This is an open access article distributed under the Creative Commons Attribution License, which permits unrestricted use, distribution, and reproduction in any medium, provided the original work is properly cited.

In this article, we take a 126 kV single-break vacuum circuit breaker as the research object and study the application of high-energy-density PM motor in the high-voltage circuit breaker for the first time. The PM motor maintains maximum power density and torque density during the start-up phase. Note that most of the faults of high-voltage circuit breakers are mechanical faults. We designed a set of mechanical fault prediction systems for high-voltage circuit breakers. We present the prediction method of the opening and closing action curve of the high-voltage circuit breaker. It is inspired by Chaos Ant Colony Algorithm (CAS) and an optimized Long- and Short-Term Memory (LSTM) cycle neural network. We constructed the main structure of the neural network expert system and established the fault prediction model of the high-voltage circuit breaker, based on the LSTM cycle neural network, optimized by CAS. We used the improved least-square method to achieve the operation accuracy of the phase control switch. Finally, we completed the development and experiment of the prototype.

1. Introduction

Presently, most of the high-voltage circuit breaker motor operating mechanisms drive motor using a permanent magnet brushless DC motor. As its back EMF waveform is a rectangular wave, and when high-speed drive noise is significant and causes resonance, it affects the control accuracy of moving contact [1–3]. Moreover, the current ripple caused by cogging torque, flux density distortion, and other factors leads to a larger torque ripple [4–6]. Therefore, this type of motor will inevitably produce a torque ripple interference in the starting phase and achieve good results in the circuit breaker of lower voltage level. However, it is not suitable for the drive motor of a high-voltage circuit breaker. In this regard, the advantages of a High-Torque and High-Power-density Permanent-magnet Motor (HTPPM) are high efficiency, high power density, and excellent control performance. These advantages make the HTPPM useful in the field of high-performance drive. The main difference between HTPPM and other motors is the structure of the

rotor magnetic circuit. The key to its design is the design of the rotor structure [7]. Herein, we analyze the actual structure and the force energy density of the permanent magnet synchronous motor with different structural parameters to improve its overload capacity.

Fault prediction of the high-voltage circuit breaker is to monitor its operation status to find a potential fault in advance. If combined with the traditional forward reasoning mechanisms, this method can diagnose the fault signal obtained by the online monitoring device quickly. Moreover, it can analyze the fault type using the existing expert experience. We add the confirmed new types of fault to the knowledge base by predefined operating procedures. [8–12].

1.1. The Operating Mechanism of the High-Power-Density Permanent-Magnet Motor. The operation process or the driving mechanism of the driving motor is presented in Figure 1. In the closing process, the motor spindle is at point A. The crank arm AB is driven to rotate at an angle α , and the

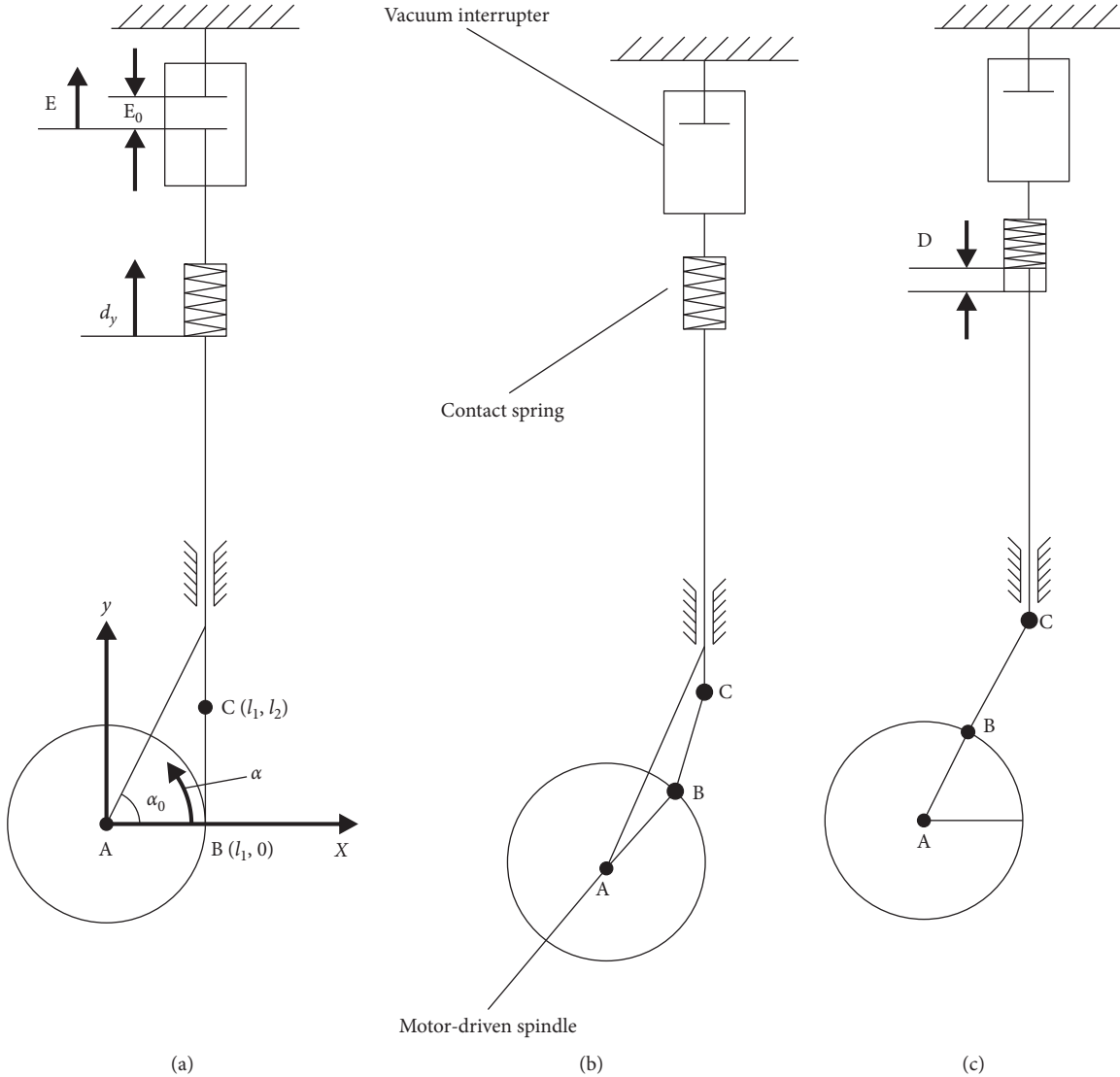


FIGURE 1: Operating principle diagram of the driving mechanism of the driving motor. (a) Opening state. (b) Rigid state. (c) Closing state.

connecting rod BC pushes the contact spring. The connected moving contact makes a straight-line movement under the rotation of the crank arm AB. The straight-line travel is E_0 . When $E = E_0$, the moving contact and the fixed contact are in a rigid closing state. If the driving motor continues to rotate at an angle α , the contact spring begins to compress. This compression happens because the dynamic and static contacts are in a rigid closing state. When $\alpha = \alpha_0$, the rotation of the drive motor is complete. The switch is in the closing state, and the compression D_1 on the contact spring is the overtravel displacement.

We obtained the relationship between the rotation angle of the driving motor linear travel of contact after thorough analysis and calculation. We found that the contact opening distance is 60 mm, the rotation angle of the motor is 33°, the overtravel is 24 mm, and the rotation angle of the motor is 35°. The relationship between the motor rotation angle and the contact stroke in the closing process is shown in Figure 2. The opening, rigid closing/rigid opening, and closing are A, B, and

C, respectively. When the motor rotates at 57.1° in the closing operation, the moving contact is in the rigid closing position. When the motor rotates at 22.9° in the opening operation, the moving contact is in the rigid opening position.

2. High-Power-Density Permanent-Magnet Motor

2.1. Basic Parameter Design. In this paper, we have designed a high-power permanent-magnet synchronous motor. The magnetic circuit structure of the motor is of a built-in type. We selected a high-performance permanent-magnet material to improve the force and energy density of the main driving motor of the high-voltage circuit breaker. The prime design parameters of the drive motor are as listed in Table 1. The length of the designed multistage drive motor core is 200 mm. Compared to the previous four-stage motor core length, the length becomes twice, the motor's weight reduces notably, and the materials used also reduce significantly.

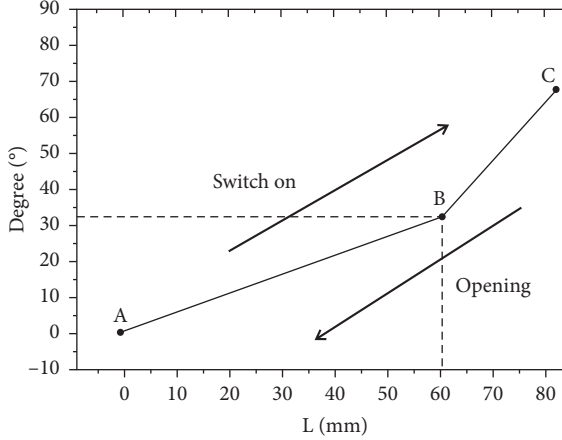


FIGURE 2: Curve of the relationship between motor angle and contact stroke.

TABLE 1: Main parameters of the driving motor.

Motor parameters	Numerical value remarks
Rated power	30 kW
Supply voltage	DC200 V
Polar logarithm	10
Core length	200 mm
Maximum speed	1000r/min
Corner range	60–80°
Magnetic load	1.4 T
Force energy density	5.1 kW•Nm/kg ² product of power density and torque density

In this paper, a shaped rotor structure, for high-power-density permanent-magnet synchronous motor, is proposed which can reduce the volume and weight and can be applied in the field of high-speed permanent-magnet motor.

There are various permanent magnet synchronous motor rotor magnetic circuit structures along with different rotor magnetic circuit structures. Their no-load magnetic flux leakage coefficient is different. It has a significant impact on improving the performance and power density of the motor. The TPPMM simulation model of the main drive is present in Figure 3 [13–16].

2.2. Optimization Design of the Magnetic Circuit Structure. In a permanent magnet motor, the total flux Φ_m , provided by the permanent magnet in the rotor to the external magnetic circuit, gets divided as the main flux Φ_δ and the leakage flux Φ_δ of the external magnetic circuit. The leakage flux gets further divided as the leakage flux existing within the axial length range of the armature core, called the interpole leakage flux $\Phi_{\delta 1}$, and the leakage flux existing outside the axial length range of the armature core, called the end leakage flux $\Phi_{\delta 2}$. The equivalent magnetic circuit of the magnetomotive force is as shown in Figure 4 following Thevenin's theorem.

As shown in Figure 4,

$$\Phi_m = \Phi_\delta + \Phi_\sigma = \Phi_\delta + \Phi_{\delta 1} + \Phi_{\delta 2}. \quad (1)$$

The pole to pole leakage coefficient is

$$\sigma_1 = 1 + \frac{\Phi_{\delta 1}}{\Phi_\delta}. \quad (2)$$

The end leakage coefficient is

$$\sigma_2 = 1 + \frac{\Phi_{\delta 2}}{\Phi_\delta}. \quad (3)$$

The ratio of the total flux to main flux is called the flux leakage coefficient of permanent magnet motor, given by

$$\sigma_0 = \frac{\Phi_m}{\Phi_\delta} = \sigma_1 + \sigma_2 - 1. \quad (4)$$

As shown in Figures 5 and 6, with the multisegment rotor structure, there exist not only interpole leakage and end leakage fluxes but also intersegment leakage flux. Due to many rotor segments and the large proportion of the total flux leakage between segments, the flux leakage between them and the end flux leakage must be fully considered and calculated.

Cogging torque is a vital parameter of the main drive motor of the high-voltage circuit breaker. Its simulated image is present in Figure 7. It can be seen that the cogging torque is 0.006 Nm, which is small, implying that the cogging effect of the designed main drive motor is small.

The torque output dynamic curve of the high-power-density permanent-magnet motor, driven by the high-voltage circuit breaker, is shown in Figure 8. We can see that the output torque in the initial stage can reach 276 nm and the output torque of the main drive motor becomes stable at 120 nm after 20 ms, which meets the requirements of the

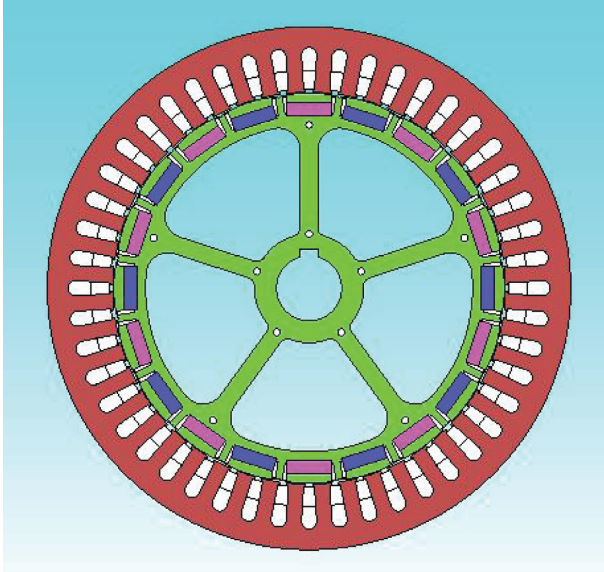


FIGURE 3: Main drive simulation model of HTPPM.

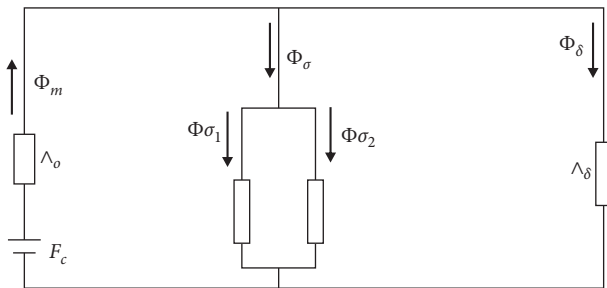


FIGURE 4: Equivalent magnetic circuit of magnetomotive force source of a permanent-magnet motor.

theoretical design value and verifies the correctness of the theoretical analysis and design.

3. Mechanical Properties of HTPPM

While making the electromagnetic design, we solved the design and calculation of the mechanical part simultaneously. Doing this ensured the economic rationality and operation reliability of motor design and manufacturing from the structure. Figure 9 shows the stress profile of the HTPPM stator core. The finite element analysis plus constraint and the radial load diagram of the HTPPM rotor structure are shown in Figure 10. We established the finite-element analysis model and then enter the finite-element analysis environment, the model mesh. According to the shape, size, and stress mode of the model, we divided the mesh. We transformed the geometric model into the finite-element model and defined the material properties. We selected the material of the model from the material library, defined its properties, and applied the load and boundary conditions. According to the force condition of the model, we applied the load, defined the constraint conditions, and output the analysis results.

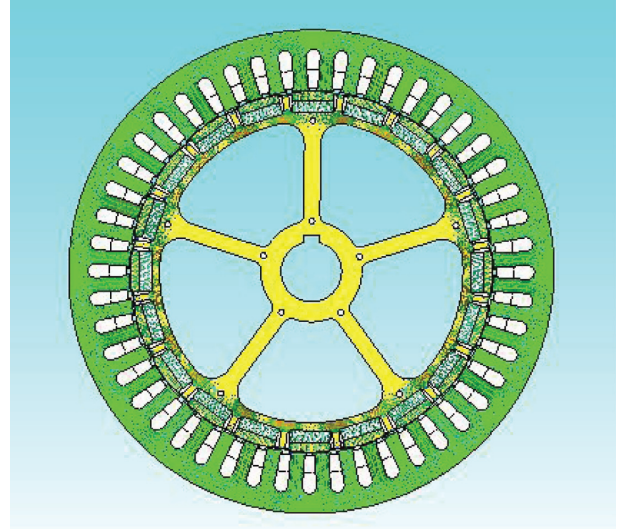


FIGURE 5: Distribution diagram of main driving magnetic field strength of HTPPM.

We calculated the high-power-density permanent-magnet synchronous motor designed in this paper when it operates at an over speed of 20% (1300 rpm). The main parameters of the rotor are as follows: the outer diameter of the rotor punching piece is $D = 548$ mm; the inner diameter is $d = 170$ mm. The material properties are as follows: elastic modulus of silicon steel sheet = 2.1×10^5 MPa, Poisson's ratio = 0.27; the elastic modulus of the permanent magnet = 1.13×10^5 MPa, Poisson's ratio = 0.23. The partial enlarged drawing of Von Mises stress contour, calculated by the noncontact finite-element method, is shown in Figure 10. We can see that the two most dangerous areas are located in the rotor slot and the magnetic isolation bridge. The maximum Von Mises stress at the slot is 232 MPa, and the maximum Von Mises stress at the magnetic isolation bridge is 206 MPa, lower than the yield stress of the silicon steel sheet used (i.e., 431 MPa), meeting the strength requirements.

4. Establishment of the Fault Prediction Model for the High-Voltage Circuit Breaker

Dynamic data for the opening and closing coil current are obtained in the operation of a circuit breaker. We can find the latent fault of the high-voltage circuit breaker to predict and realize the future values. We use $Y(t)$ to represent the operation curve of the opening and closing coil current of the circuit breaker. Since every action of the circuit breaker is not continuous and the time interval between each operation is long, every operation is taken as a sample $Y(t - n + 1), \dots, Y(t - 1), Y(t)$ of the current feature data of the opening and closing coils. At n consecutive times, it is taken as the input, and $Y(t + 1)$ is taken as the output of the prediction model, where n corresponds to the number of input layers. The mathematical expression of the prediction model is

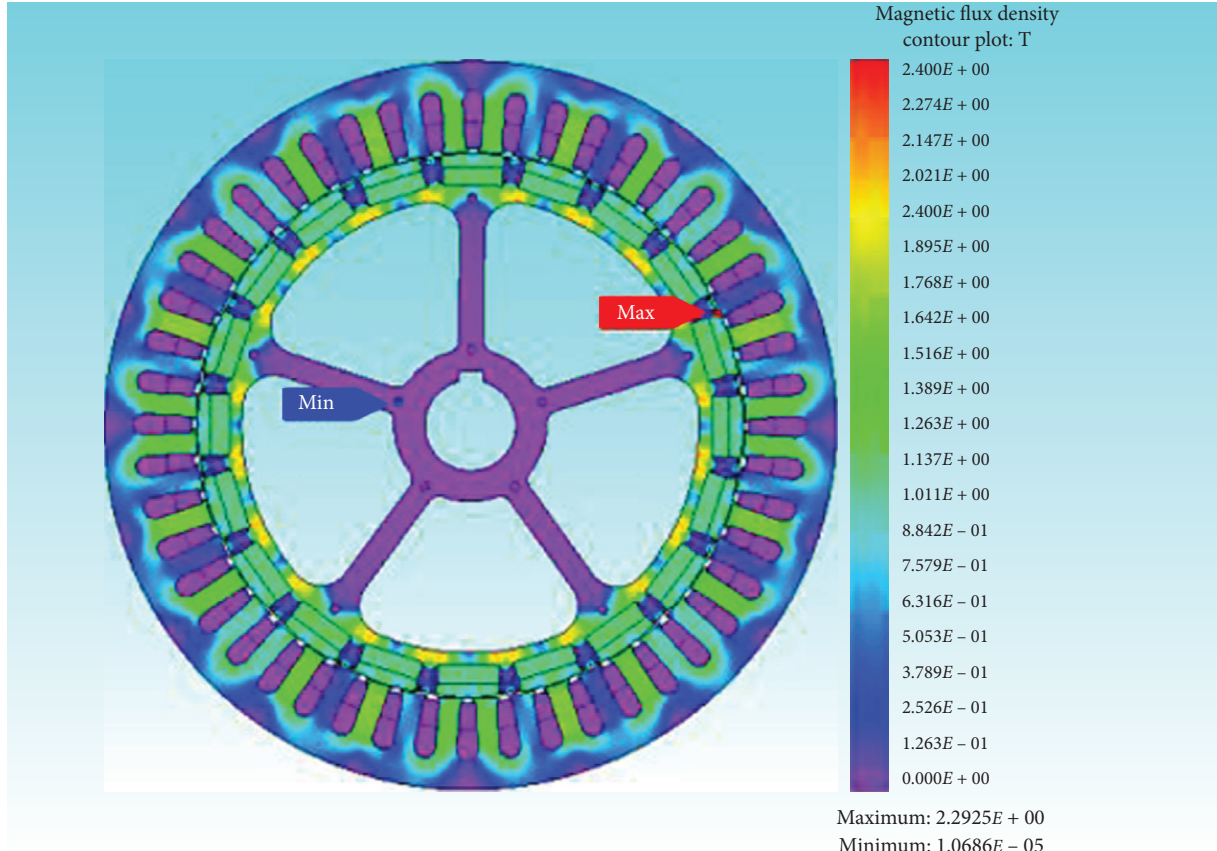


FIGURE 6: Simulation diagram of no-load magnetic density distribution of main drive of HTPPM.

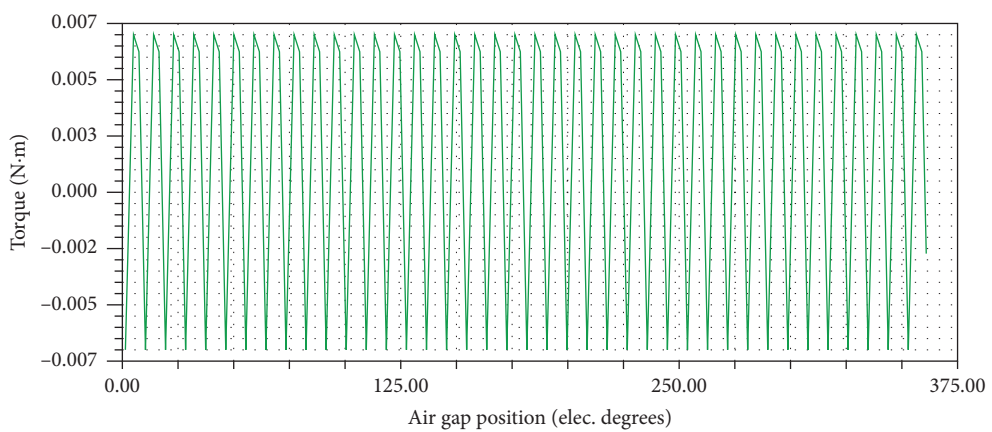


FIGURE 7: Cogging torque.

$$Y(t+1) = \int (\{Y(t-n+1), \dots, Y(t-1), Y(t)\}). \quad (5)$$

4.1. Establishment of the Model. Unlike the input of the general neural network, the input of the LSTM recurrent neural network is a time series, input in the form of a tensor. The training accuracy of the network also differs while taking different input batch data. The number of LSTM units used has a direct impact on the prediction

accuracy of the model during the training. If we choose too little, the model will appear to be underfitting; it may not fit the stroke curve well. If we choose too much, it will appear to be overfitting; it will affect the generalization ability of the model. Currently, there is no clear method to select the number of hidden-layer elements obtained by the empirical formula. The number of hidden-layer elements with the smallest prediction error is selected as the prediction model by the formula primary selection with a slight increase or decrease. [17–20].

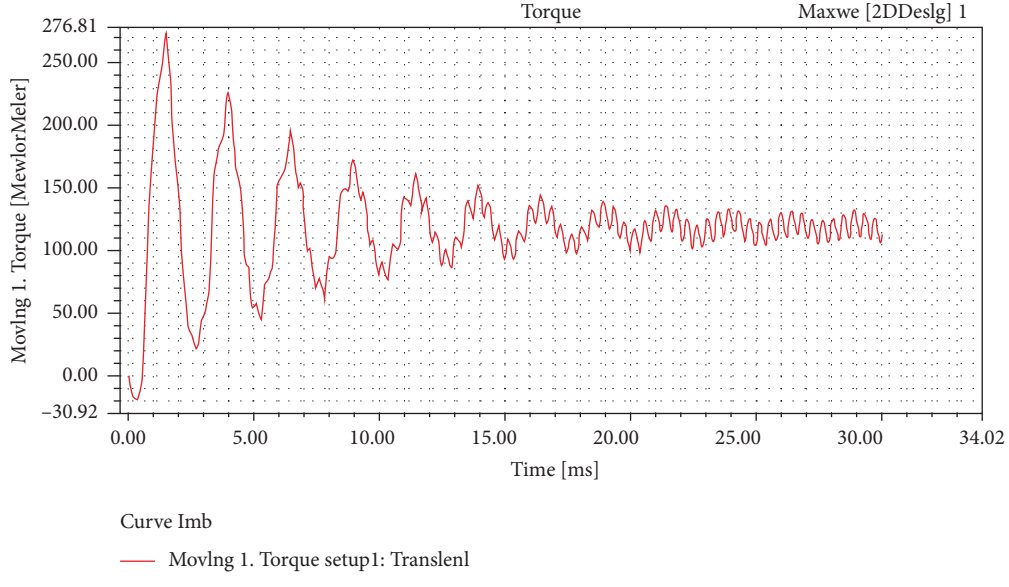


FIGURE 8: Motor output torque.

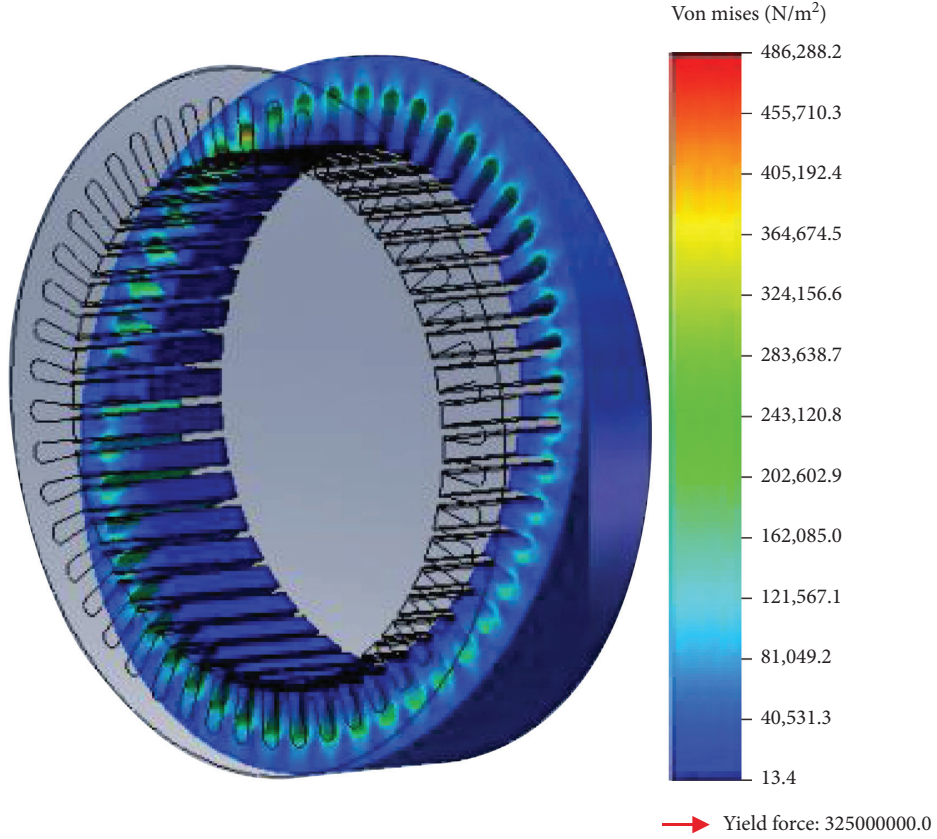


FIGURE 9: Sectional view of stator core stress of HTPPM.

$$M = \sqrt{(n + m)} + z. \quad (6)$$

In equation (6), m and n are the number of nodes in the input and output layers and Z is the constant in $[0, 10]$.

4.2. Building a Fault Prediction Model under the TensorFlow Framework. We select 600 groups of samples. Each group of specimens is 40 sampling points. We divide them into 300, 150, and 150 training sets, test sets, and verification sets,

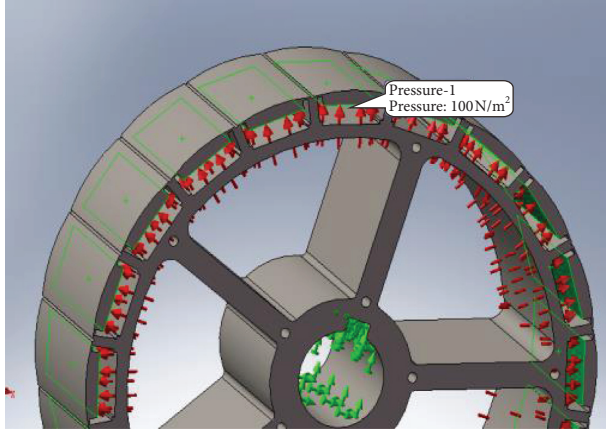


FIGURE 10: Finite element analysis of the rotor structure with constraints and radial loads of HTPPM.

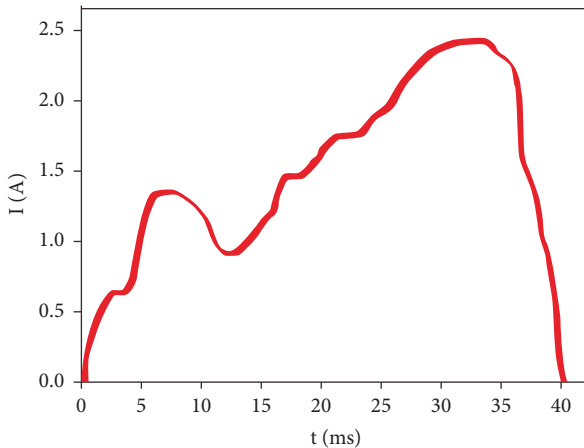


FIGURE 11: Current waveform of the opening coil.

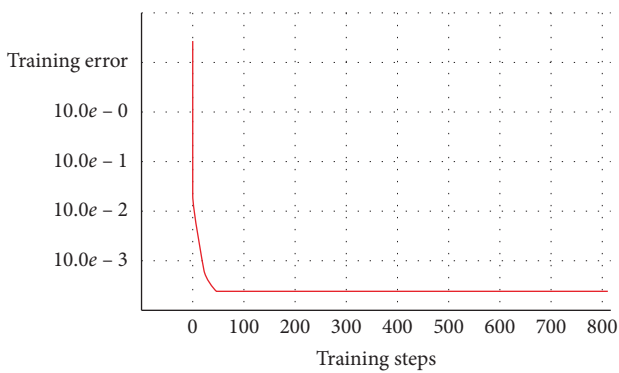


FIGURE 12: Loss value of training function.

respectively. The current action curves of the opening and the closing coil of the circuit breaker are shown in Figure 11.

The training process of the CAS-optimized LSTM prediction model is as shown in Figure 12. We can see from Figure 12 that the training error of the model is small at

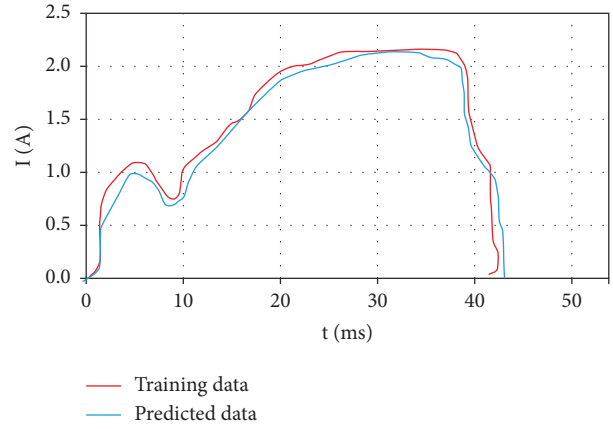


FIGURE 13: Forecast curve results.

about 50 steps. Due to the GPU version of TensorFlow simulation training, the average training time of an 800-step model is less than 12 min.

The prediction model is used to predict the opening and the closing coil current in time series, and the prediction results are as shown in Figure 13. From Figure 13, it is clear that the model can effectively determine the opening and closing coil current of the circuit breaker, and the prediction curve can accurately reflect the characteristics of each stroke of the circuit breaker, which can be used as the basis for fault determination of the circuit breaker.

5. Conclusions

- (1) The high-power motor of the high-voltage circuit breaker and motor operating mechanism are analyzed as the operating mechanisms of the high-voltage circuit breaker. By analyzing the relationship between motor angle and contact stroke, the working characteristics of a permanent-magnet motor with the high power density and high-power motor are developed.
- (2) By optimizing the design of the magnetic circuit, we provided the cogging torque simulation diagram and the motor output torque dynamic curve to fulfill the performance requirements of the high-voltage circuit breaker. We established the finite-element analysis model, and the stress profile of the HTPPM stator core and the finite element analysis of the HTPPM rotor structure with constraints and radial loads were given, which meet the strength requirements.
- (3) We established the model of fault prediction for a high-voltage circuit breaker. Through the loss value of the training function and the resulting chart of the prediction curve, we verified that CAS optimization training the LSTM recurrent neural network is an effective method.

Data Availability

The analysis result data used to support the findings of this study are included within the article.

Conflicts of Interest

The authors declare that they have no conflicts of interest.

References

- [1] X. Lin, *Permanent Actuator and Vacuum Circuit Breaker*, Mechanical Industry Press, Beijing, China, 2011.
- [2] G. ZhanG, *Theoretical Basis of Electrical Appliances*, Mechanical Industry Press, Beijing, China, 1997.
- [3] Y. Ma, *Research of HCB Novel Motor Operating mechanism*, Shenyang University of Technology, Shenyang, China, 2008.
- [4] C. Qiao, *Research on the Design of Asymmetric Winding Motor Mechanism of High Voltage disconnector*, Shenyang University of Technology, Shenyang, China, 2012.
- [5] Y. Li, *Research on the Operating Mechanism of Permanent Magnet Motor for 126kV High Voltage Vacuum Circuit breaker*, Shenyang University of Technology, Shenyang, China, 2013.
- [6] L. Wang, J. Xu, and X. Lin, "Research on control technology of motor operating mechanism of high voltage circuit breaker," in *Proceedings of the 2012 Annual Meeting of Power Transmission and Transformation*, pp. 95–100, Sinaia, Romania, June 2002.
- [7] S. Wang, *Research on Key Technology of High Power Density Permanent Magnet Motor for UAV Main Propulsion*, Shenyang University of Technology, Shenyang, China, 2014.
- [8] X. Fan, F. Meng, C. Fu et al., "Research of brushless DC motor simulation system based on RBF-PID algorithm," in *Proceedings of the Second International Symposium on Knowledge Acquisition and Modeling*, pp. 277–280, IEEE Computer Society, Wuhan, China, December 2009.
- [9] C. Akman, S. Haider, Y. Ayarcan et al., "Anti-windup PID controller with integral state predictor for variable-speed motor drives," *IEEE Transactions on Industrial Electronics*, vol. 59, no. 3, pp. 1509–1516, 2012.
- [10] Z. Chen, *Research on Intelligent Neural Network Control of Linear Permanent Magnet Synchronous Motor Servo system*, Jiangxi University of Technology, Ganzhou, China, 2011.
- [11] W. Zhou, *Research on Hidden Layer Structure and Parameter Optimization of RBF Neural network*, East China University of Science and Technology, Shanghai, China, 2014.
- [12] K. Huang, Z. Yu, Q. Dong et al., "Research on self-tuning PID control based on BP neural network of multi-motor synchronous control system," *Advanced Science Letters*, vol. 19, no. 6, pp. 1668–1671, 2013.
- [13] J. Wang, F. Wang, X. Kong et al., "Design and electromagnetic performance analysis of high speed permanent magnet generator," *Proceedings of the CSEE*, vol. 28, no. 20, pp. 105–110, 2008.
- [14] X. Wang, Z. Jia, and P. Gao, "Coupled solution analysis of electromagnetic field and temperature field of outer rotor hub motor," *Journal of Tianjin University*, no. 10, pp. 898–902, 2014.
- [15] S.-T. Lee, H.-J. Kim, J.-H. Cho, D.-S. Joo, and D.-K. Kim, "Thermal analysis of interior permanent-magnet synchronous motor by electromagnetic field-thermal linked analysis," *Journal of Electrical Engineering and Technology*, vol. 7, no. 6, pp. 905–910, 2012.
- [16] M. Chen, G. Zhang, and W. Hua, "A summary of stator permanent magnet brushless motor system and its key technologies," *Proceedings of the CSEE*, vol. 34, no. 29, pp. 5204–5220, 2014.
- [17] X. Wang, J. Wu, C. Liu, H. Yang, Y. Du, and W. Niu, "Fault time series prediction based on LSTM recurrent neural network," *Journal of Beijing University of Aeronautics and Astronautics*, vol. 44, no. 4, pp. 772–784, 2018.
- [18] Y. Li, *Chaos Ant Colony Optimization Algorithm and its application*, Beijing University of Posts and Telecommunications, Beijing, China, 2009.
- [19] Z. Pei, *Improvement and Application of Ant Colony algorithm*, Liaoning University of science and technology, Shenyang, China, 2015.
- [20] A. Chen, B. Zhou, H. Zhang et al., "Mechanical fault clustering diagnosis method based on PCA and ant colony algorithm," *China Mechanical Engineering*, vol. 3344, pp. 3333–3337, 2013.